

Modeling and experimental characterization of stepped and v-shaped $\{311\}$ defects in silicon

Luis A. Marqués* and María Aboy

*Departamento de Electrónica, Universidad de Valladolid,
E.T.S.I. de Telecomunicación, 47011 Valladolid, Spain*

Karleen J. Dudeck and Gianluigi A. Botton

*Department of Materials Science and Engineering,
McMaster University, 1280 Main Street West,
Hamilton, Ontario L8S 4L7, Canada*

Andrew P. Knights

*Department of Engineering Physics,
McMaster University, 1280 Main Street West,
Hamilton, Ontario L8S 4L7, Canada*

Russell M. Gwilliam

*Surrey Ion Beam Centre, University of Surrey,
Guildford, Surrey, GU2 7XH, U.K.*

Abstract

We propose an atomistic model to describe extended $\{311\}$ defects in silicon. It is based on the combination of interstitial and bond defect chains. The model is able to accurately reproduce not only planar $\{311\}$ defects, but also defect structures that show steps, bends or both. We use molecular dynamics techniques to show that these interstitial and bond defect chains spontaneously transform into extended $\{311\}$ defects. Simulations are validated by comparing with precise experimental measurements on actual $\{311\}$ defects. The excellent agreement between the simulated and experimentally derived structures, regarding individual atomic positions and shape of the distinct structural $\{311\}$ defect units, provides strong evidence for the robustness of the proposed model.

PACS numbers: 61.72.Cc, 61.72.Nn, 61.43.Bn, 68.37.Ma

I. INTRODUCTION

Defect engineering in semiconductors is a topic of great interest. Ion implantation and annealing are key processing steps used for the fabrication of PN junctions within the manufacturing industry of Si and Ge electronic devices. Besides the introduced dopant atoms, excess self-interstitials above equilibrium conditions are generated in the lattice. They form aggregates that evolve through an Ostwald ripening process: larger defect clusters grow at the expense of single interstitials freed from smaller and less stable agglomerates.¹ At sizes of several hundred interstitials these aggregates become visible in transmission electron microscopy (TEM) images, they show regular atomic structures, and are generally known as *extended defects*.^{2,3} The type of defects which can be observed depends on the implantation and annealing conditions. Most common in Si are the so-called $\{311\}$ defects, the $\{111\}$ rod-like defects, and the Frank and perfect dislocation loops, which lie in a $\{111\}$ plane.^{4,5} While not common in Si, extended planar $\{001\}$ aggregates have also been observed in Ge.² Some of these defects show photoluminescent signals and have been proposed to fabricate optical emitters compatible with the standard and well-established integrated-circuit technology.^{6,7}

Among interstitial-rich extended defects, $\{311\}$ defects have received much attention because they are formed during implantation and annealing conditions relevant to Si processing. They act as a reservoir of interstitials that are slowly released during subsequent thermal treatments causing the transient enhanced diffusion (TED) of interstitial-diffusing dopants.⁸ The atomic structure of $\{311\}$ defects was determined by Takeda using TEM.⁹ It consists of large interstitial chains along the $\langle 110 \rangle$ direction, packed together along the $\{311\}$ plane, which gives this defect its name. Its atomic model can be described as a sequence of structural units of three types: *I units*, which are two tiny rods of hexagonal Si containing the interstitial $\langle 110 \rangle$ chains; *O units*, 8-member rings with no excess nor deficit of atoms with respect to perfect lattice; and *E units*, 7-member rings at the defect boundaries.¹⁰ These units also show five-member rings which act as an interface between the $\{311\}$ defect and the surrounding perfect crystal. Usually ion implantation and annealing lead to the formation of long and narrow $\{311\}$ defects, while high-dose electron irradiation produces much wider structures.^{3,9} Apart from the perfectly planar $\{311\}$ defects, structures with steps and bends have also been observed.¹¹

Due to the technological relevance of extended $\{311\}$ defects, it would be desirable to

have an atomistic model, simple enough but with predictive capabilities, able to reproduce the different structures they can adopt. A number of theoretical investigations on the $\{311\}$ defect based on first-principles and tight-binding calculations, regarding its structure, energetics, and induced strain fields, have been published.^{10,12–15} In all these studies the atomic configurations of $\{311\}$ defects were used as an input. Consequently, these calculations are not able to explain how extended $\{311\}$ defects generate from simpler agglomerates. Creation of $\{311\}$ defects as the result of the coordinated generation of long interstitial chains and switching of atomic bonds, as it has been proposed,^{10,15} seems rather unrealistic.

In a previous paper we proposed an atomistic model for the description and formation of planar $\{311\}$ defects based on chains of self-interstitials and bond defects (BDs).¹⁶ By the use of classical molecular dynamics (MD) techniques, we showed that these precursor chains are metastable and spontaneously transform into planar $\{311\}$ defects when annealed at high temperatures. The only assumption in our simulations was the exact nature of the precursors, based on the fact that chains of self-interstitials and BDs in a Si lattice naturally follow a $\{311\}$ plane. Recently we compared the simulation results with experimental measurements obtained by high-angle annular dark-field (HAADF) scanning TEM (STEM) images.¹⁷ Agreement between experiment and theoretical atomic positions was better than ± 0.05 nm. It was also found that the shape of five-, six-, seven- and eight-member rings in $\{311\}$ defect units varies as a function of position within the defect, and that was perfectly reproduced in the simulations. In the present paper we extend the validity of our atomistic model to also reproduce stepped and bent (v-shaped) $\{311\}$ defects. Experimental characterization of these defects is also carried out in order to compare and validate the model.

The paper is organized as follows. In Sec. II we briefly describe the basis of our atomistic model. The experimental setup used to generate, identify and characterize extended $\{311\}$ defects with steps and bends is described in Sec. III. In Sec. IV we show our simulation results reproducing the particular structures observed in the experiments, with a detailed comparison between theory and measurements. Finally the main conclusions are summarized in Sec. V.

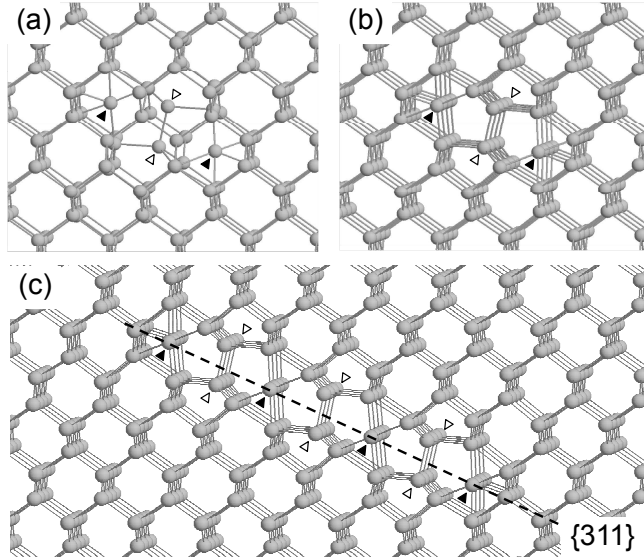


FIG. 1: Ball and stick models of: (a) the Si di-interstitial, (b) a linear defect with one BD chain and two Si interstitial chains, and (c) a planar defect with three BD chains and four Si interstitial chains. Solid and open triangles indicate Si interstitials and BD atoms, respectively.

II. DESCRIPTION OF THE MODEL

Our model is based on the combination of self-interstitials and BDs. The BD consists of a local rearrangement of bonds in the semiconductor lattice without any excess or deficit of atoms.^{18,19} It has been shown that when two Si self-interstitials interact to form a di-interstitial, a BD is generated between them, which lowers the formation energy with respect to the corresponding two individual interstitials.²⁰ A ball and stick model of the Si di-interstitial is shown in Fig. 1(a). This result was obtained with MD simulations using the Tersoff 3 potential to describe silicon interactions.²¹ However, the structure of the Si di-interstitial does not seem to depend on that particular interatomic potential, as it has been also predicted as a stable Si di-interstitial configuration by the Stillinger-Weber potential²² and first-principle calculations.^{23,24}

By repeating the Si di-interstitial structure (interstitial-BD-interstitial), extended defects can be generated. In Fig. 1(b) we show a defect generated by repeating the di-interstitial structure along the $\langle 110 \rangle$ direction. It can be described as two rows of interstitial atoms and one row of BDs in between. Analogously, additional BDs and Si interstitials can be added at both sides. This procedure generates planar defects as the one shown in Fig.

1(c). Interestingly enough, its habit plane is precisely the $\{311\}$ plane. In a previous paper we demonstrated that these interstitial and BD chains form metastable structures in the Si lattice, which spontaneously transform into $\{311\}$ defects when annealed at high temperatures.¹⁶

These simulation results suggest a possible pathway for the formation of extended $\{311\}$ defects from simpler agglomerates. Following implantation and during annealing, self-interstitials start to diffuse and interact to form small defect clusters.²⁵ Some of them are fast-diffusing species, such as the di- and tri-interstitial, as it has been demonstrated using *ab initio* techniques.²⁶ On the other hand, the compact tetra-interstitial structure is immobile and fairly stable.²⁷ The compact tetra-interstitial structure appears to be the nucleation site for $\{001\}$ planar defects. However, the case of $\{311\}$ defects is not so clear, but our simulation results suggest that they can be formed when Si di-interstitials accumulate along the $\langle 110 \rangle$ direction. In fact, it has been postulated that following implantation and/or during the ramping-up of the anneal most interstitial defects in Si are in the form of di-interstitials.²⁸ From TED experiments, it has been suspected that precursors of $\{311\}$ defects might exist with binding energies intermediate between those of the di-interstitials and of extended defects.²⁹ These precursors could be the metastable di-interstitial $\langle 110 \rangle$ chains of our model.

III. EXPERIMENTAL

Experimental sample material was prepared by implanting $1 \times 10^{15} \text{ cm}^{-3}$ indium ions into n-type (100) Si with an energy of 40 keV and an angle of 7° to the surface normal. These conditions produce an amorphous layer approximately 50 nm thick. Following implantation, the sample was annealed at 600 °C for 2 minutes in a N₂ atmosphere. This resulted in the formation of end-of-range defects at a depth commensurate with the amorphous-crystalline interface. Electron microscopy specimens were prepared by tripod polishing combined with low voltage ($< 800 \text{ V}$) ion milling, as described in Ref. 30.

HAADF STEM imaging was performed using a FEI-Titan 80-300 STEM operated at 200 keV and equipped with two aberration correctors. A convergence angle of 19 mrad and detector inner semiangle of 75 mrad were employed. Experimental images were obtained in the $[0\bar{1}\bar{1}]$ direction and oriented such that the X and Y axes were parallel to $[0\bar{1}1]$ and

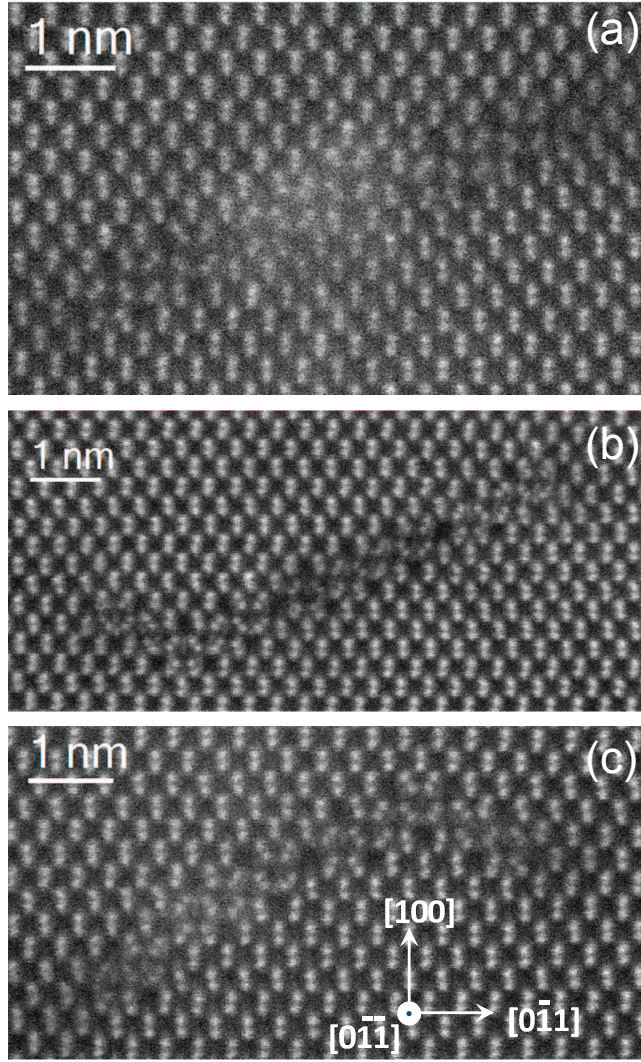


FIG. 2: Unprocessed HAADF STEM images of extended $\{311\}$ defects. (a) Stepped defect structure; (b) v-shaped defect structure; (c) v-shaped structure with a step. The crystallographic coordinate system used for experimental data analysis is shown as an inset in (c).

$[100]$, respectively. Electron energy loss spectroscopy was used to determine a specimen thickness of (25 ± 5) nm in the region of the $\{311\}$ defect using the mean-free path of total inelastic scattering.³¹ Figure 2 presents the HAADF STEM images of three extended $\{311\}$ structures: (a) a stepped defect structure; (b) a v-shaped defect structure; (c) a v-shaped structure with a step.

TABLE I: Features of the cells used in MD simulations.

Cell	X axis orientation	Y axis orientation	Z axis orientation	X size (\AA)	Y size (\AA)	Z size (\AA)	Number of atoms
C1	$[2\bar{3}\bar{3}]$	$[311]$	$[0\bar{1}1]$	127.4	93.5	23.0	13752
C2	$[0\bar{1}1]$	$[100]$	$[0\bar{1}\bar{1}]$	119.1	76.0	23.0	10512
C3	$[0\bar{1}1]$	$[100]$	$[0\bar{1}\bar{1}]$	96.0	70.7	23.0	7872

IV. RESULTS

A. MD simulations

In order to compare with the experimentally observed $\{311\}$ structures, three different simulation cells were prepared: the first (C1) for the stepped defect, second (C2) for the v-shaped, and third (C3) for the defect that shows both a step and a bend. Starting from the perfect Si lattice, we introduced 10 BD rows and 12 interstitial rows in C1, 13 BD rows and 16 interstitial rows in C2, and 9 BD rows and 12 interstitial rows in C3, always following the extended defect geometries found in the experimental images. The specific features of each simulation cell are summarized in Table I. These three cells were annealed using a classical MD simulation scheme.³² We applied periodic boundary conditions along the X and Z axes, and free boundary conditions along the Y axis for allowing the volume relaxation of the MD cells. Cell sizes in Z direction are the same in all cases (23.0 \AA), which correspond to six lattice periods. By running MD simulations in thicker cells, we have tested that such a small number of lattice periods in Z direction does not introduce finite size effects.

We used the Tersoff 3 potential to describe Si atomic interactions.²¹ This potential has been shown to give a good description of both point defects and Si structures different from the lowest energy tetrahedral diamond lattice.^{33–36} We have carried out annealing simulations at a temperature of 1400 K. Taking into account that Tersoff 3 predicts a crystal Si melting temperature of 2400 K,³⁷ a Tersoff 3 temperature of 1400 K would be equivalent to a real temperature of around 700°C, of the order of temperatures typically used in Si anneal experiments.³ Besides, high temperatures imply faster dynamics that allow obtaining meaningful results in a reduced amount of simulation time.

During annealing, and due to the structural transformation, energy is freed in the form of latent heat. If no special care is taken to eliminate such excess heat (that in real silicon would dissipate through the lattice), it remains within the MD cell due to periodic boundary

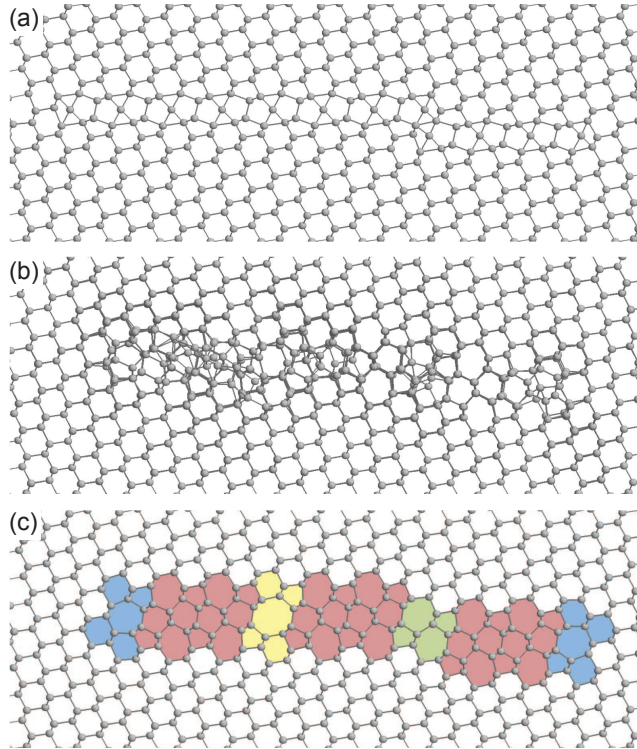


FIG. 3: (color online) XY snapshots taken during annealing at 1400 K of MD cell C1: (a) initial configuration, (b) at 1.2 ns, and (c) final configuration at 3 ns. Colors in the final defect indicate the structural units: red for I units, yellow for the O unit, blue for E units and green for the S unit.

conditions. To avoid such an artificial temperature increase, atom velocities were re-scaled every 1000 time-steps to maintain a constant temperature in the cell. We have used the fourth order Gear predictor-corrector algorithm to integrate equations of motion.³⁸

Figures 3, 4 and 5 represent several XY snapshots taken during the annealing simulations of cells C1, C2 and C3, respectively, showing the structural transformation from the initial interstitial and BD rows to the final extended $\{311\}$ defects found in the experiments. These defect structures behave as if being of infinite length along the $\langle 110 \rangle$ direction since, as we mentioned above, periodic boundary conditions are applied in Z . From the last snapshots it is easy to identify the very well known E, I and O units. Apart from them, it is also possible to identify the structural units that build steps and bends. Final defect in C1 shows a step (see Fig. 3(c)) which consists on two five-member rings and two seven-member rings. We will refer to this particular atomic arrangement as an S unit. The final defect in C3 also shows a step (see Fig. 5(c)), but the arrangement of five- and seven-member rings in that

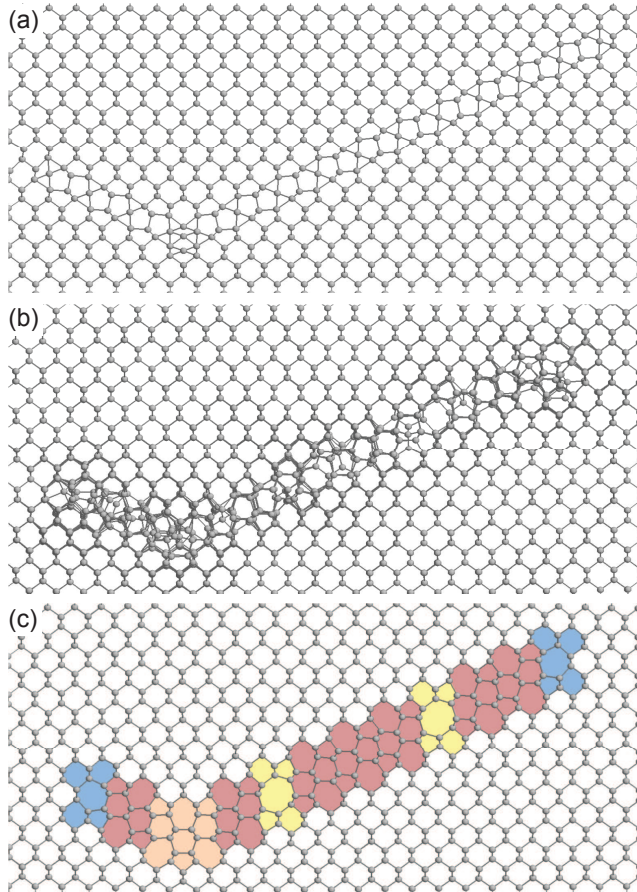


FIG. 4: (color online) XY snapshots taken during annealing at 1400 K of MD cell C2: (a) initial configuration, (b) at 0.8 ns, and (c) final configuration at 2.4 ns. Colors in the final defect indicate the structural units: red for I units, yellow for O units, blue for E units and orange for the V unit.

step, which we will refer to as an S' unit, is different with respect to the S unit. Defects in C2 and C3 show a bend (Figures 4(c) and 5(c)), whose particular atomic arrangement is the same in both cases, consisting in three seven-member rings, three six-member rings typical of a hexagonal lattice, and three five-member rings. We will refer to this structure as a V unit. The S and V units were already considered in the tight-binding calculations of Kim *et al.* and Alippi and Colombo.^{13,14} However, and as far as we know, the S' unit has not yet been reported. Following the notation usually employed to describe $\{311\}$ extended defects, the structure of defects found after annealing of C1, C2 and C3 are EIIOIISIIE, EIVIOIIOIIE and EIS'IIOIVIE, respectively.

In Fig. 6 we present simplified schematics of the transformations from the interstitials and BD rows to the final $\{311\}$ defect structures. During the MD annealing simulations,

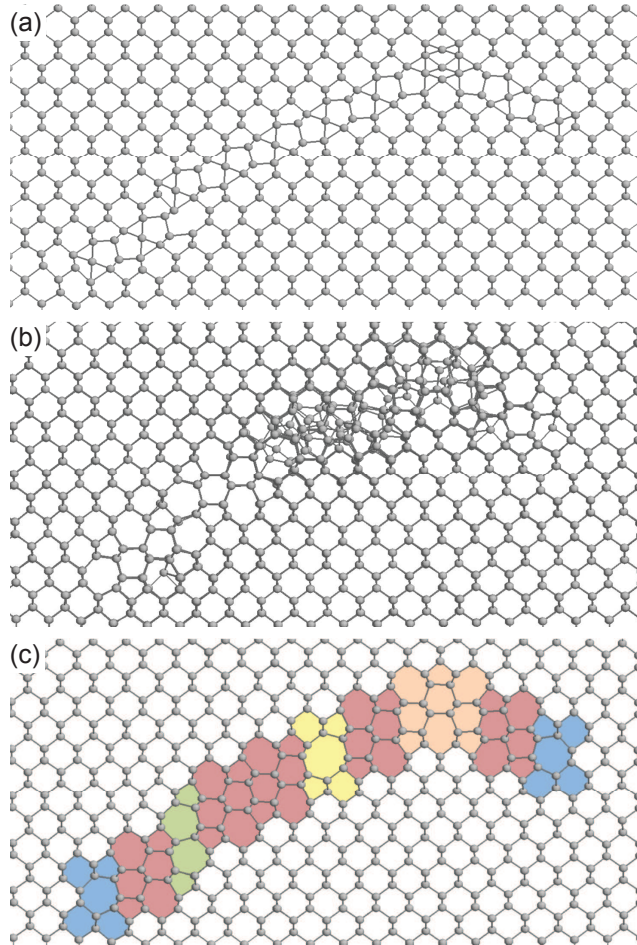


FIG. 5: (color online) XY snapshots taken during annealing at 1400 K of MD cell C3: (a) initial configuration, (b) at 0.8 ns, and (c) final configuration at 2 ns. Colors in the final defect indicate the structural units: red for I units, yellow for the O unit, blue for E units, green for the S' unit and orange for the V unit.

interstitial atoms move along the defect and reorganize their positions following the arrows indicated in Fig. 6(b). Interstitial atoms reorganize further trying to find the local potential energy minima, as shown in Fig. 6(c). Isolated BD rows remain at the left side of the C1 defect and at both sides of C2 defect. These isolated BD rows later recombine and perfect lattice is recovered at the defect sides. This produces the narrowing of the extended defects in C1 and C2 with respect to the initial configuration of BD and interstitial rows. The same result was observed in previous simulations involving planar $\{311\}$ defects.¹⁶ Our atomistic model predicts a 50% ratio between I and O units, but in fact the defect width shrinks during the transformation to a final higher ratio between I and O units. This is in fair

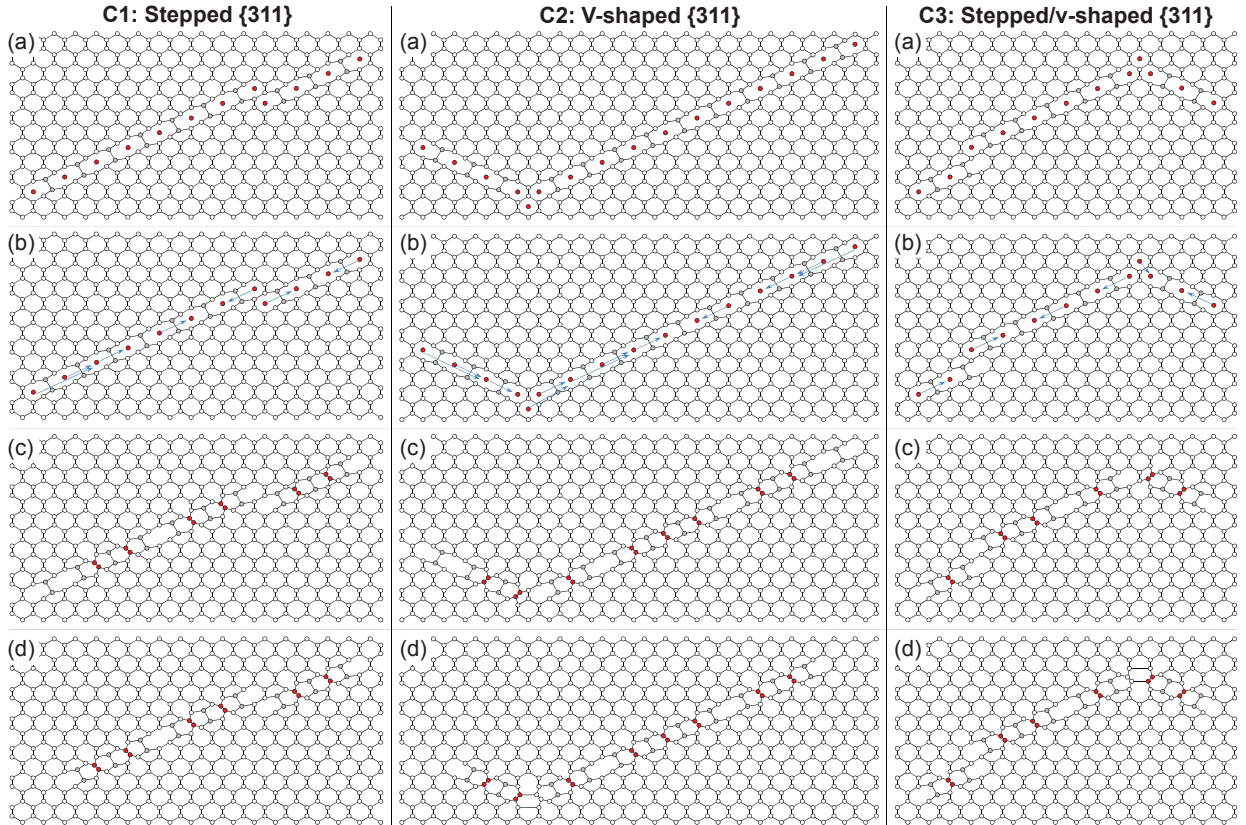


FIG. 6: (color online) Schematics for the structural transformations observed in the MD simulations: (a) starting configurations with interstitial (red) and BD (gray) rows, (b) interstitial atoms move along the defect following the indicated arrows, (c) interstitial atoms reorganize further trying to find the local potential energy minima, and (d) isolated bond defect rows at sides recombine, while some bond reorganization takes place at defect bends.

agreement with experiments, where a ratio of 62% has been found in wide $\{311\}$ defects.⁹ Theoretical calculations have shown that the separation of O units between one, two or three I units observed in TEM acts to relax the strain energy introduced in the Si lattice by the I units.^{10,14} In Fig. 6(d) we show the final configurations where some further atomic rearrangements have taken place at the vertex of C2 and C3 defects. From these schematics it is easy to realize that S and S' units have no excess atoms with respect to the perfect lattice. However, V units do introduce two extra interstitial rows in the lattice as it is the case of I units. It is worth noting here that these are only simplified rearrangement schemes, since in practice atoms move significantly along the Y direction and some of them in the Z direction as well. Apart from the BDs that end up isolated at the defect sides, positions of

BDs are not altered along the structural transformation, although their constituent atoms can be exchanged during annealing by atoms that previously occupied interstitial or perfect lattice positions.

B. Experimental-theoretical comparison

In order to compare the experimental defect structures with the theoretical structures, atomic column positions were determined from the experimental images using the procedure outlined in Ref. 17. In brief: X and Y axes were defined parallel to $[0\bar{1}1]$ and $[100]$, respectively; atomic column positions $\mathbf{r} = (x, y)$ were determined by fitting two-dimensional Gaussians to each peak position and the x- and y-standard deviations (σ_x and σ_y , respectively) of the Gaussian fit were taken as the uncertainty in the experimental peak positions. No distortion correction or averaging was performed on the HAADF STEM images prior to or during comparison with theoretical data. The positions of the atomic columns from the MD simulation were determined by averaging the x- and y-coordinates of atoms on each column in the modeled structures. Experimental peak positions were aligned to the theoretical positions using the Procrustes transformation.³⁹ In the case of the stepped defect, 420 column positions (134 columns associated with the defect and 286 columns associated with the bulk) were used to align the data, while 618 column positions (172 from the defect and 446 from the bulk) and 432 column positions (142 from the defect and 290 from the bulk) were used to align the v-shaped and stepped/v-shaped defects, respectively.

The aligned experimental and theoretical peak positions from the stepped, v-shaped and stepped/v-shaped defects are shown in Figs. 7(a), 8(a) and 9(a), respectively. The theoretical derived structures agree with the experimental structures in all cases. Considering all three defect structures, 1470 column positions compared (448 columns associated with defect structures and 1022 associated with the bulk), 1458 sets agreed within ± 0.05 nm, which is the average uncertainty in the experimental position and within 95% confidence (12 sets had separations between 0.05 and 0.1 nm). In addition to comparing absolute column position, the side lengths and inner angles of all of the five-, six-, seven- and eight-member rings were compared for the three structures. For all three defect structures, the mean difference between the experimental and theoretical side lengths was (0 ± 0.02) nm (considering only unique side lengths) and the mean difference between inner angles was $(0 \pm 12)^\circ$.

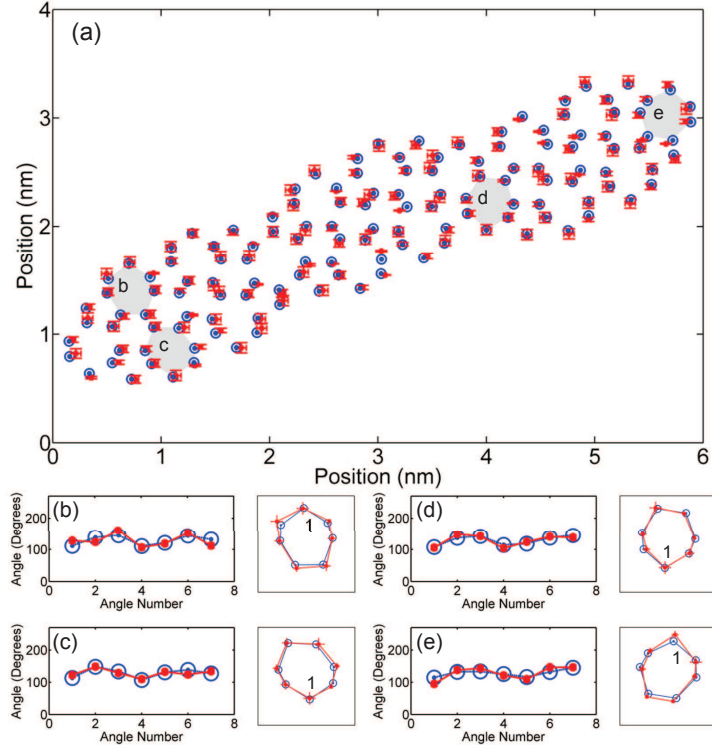


FIG. 7: (color online) (a) Structural units associated with the stepped defect measured from the experimental column positions (red \odot) and aligned to theoretical column positions (blue \odot). Error bars on experimental positions represent σ_x and σ_y of the Gaussian fit. Four seven-member rings (labeled (b)–(e)) are highlighted on (a). (b)–(e) The inner angles and detailed structural comparison for the seven-member rings as labeled in (a). Inner angles are numbered in a clockwise direction starting from one, as indicated in the structural comparison plots. The boxes containing the structural comparison plots are 0.4 nm square. All experimental points in (a) are plotted with error bars, though they may appear within the plot symbols. In (b)–(e) solid red and dashed blue lines connecting experimental and theoretical data points (respectively) have been added as a guide for the eye.

Structural variations of the different five-, six-, seven- and eight-member rings along the defects were of particular interest. We compared the side lengths, inner angle magnitudes and overall shape of the different ring structures along the length of the three defects (examples of this type of data comparison can be found in Ref. 17). Subtle structural variations in the five- and seven-member rings were observed along the length of the defects for all three defects, for example different aspect ratios or distortions. These variations were observed

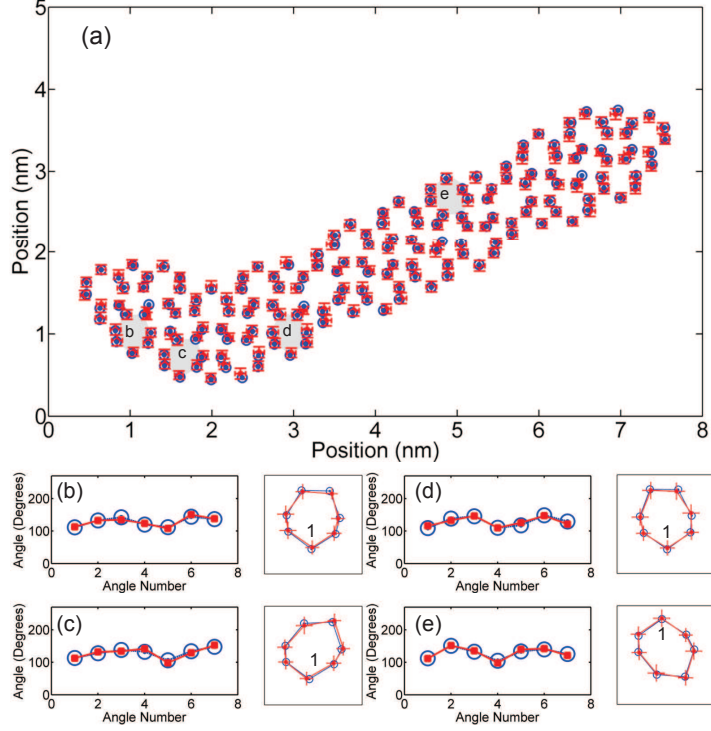


FIG. 8: (color online) (a) Structural units associated with the v-shaped defect measured from the experimental column positions and aligned to theoretical column positions. Four seven-member rings (labeled (b)–(e)) are highlighted on (a). (b)–(e) The inner angles and detailed structural comparison for the seven-member rings as labeled in (a). The boxes containing the structural comparison plots are 0.4 nm square. Plot symbols, error bars and angle number are as in Fig. 7.

in both the experimental and theoretical data and are readily observable by analyzing the variation of inner angles as a function of position within the different ring structures. For this analysis, the inner angles were numbered from one to seven in a clockwise direction, such that the first angle was in the same position relative to the shape/symmetry of the ring. Considering the seven-member rings, four unique ring structures were observed in both the stepped and v-shaped defects (shown in Figs. 7(b)–(e) and 8(b)–(e), respectively), while five unique ring structures were observed in the stepped/v-shaped defect (shown in Fig. 9(b)–(f)). Similarities between seven-member rings from the different defects can also be noted, for example the rings shown in Figs. 7(b), 8(d) and 9(d) show the same trend in inner angle. In all cases the theoretical ring structures show the same trends in inner angle and overall ring shape as the experimental ring structures.

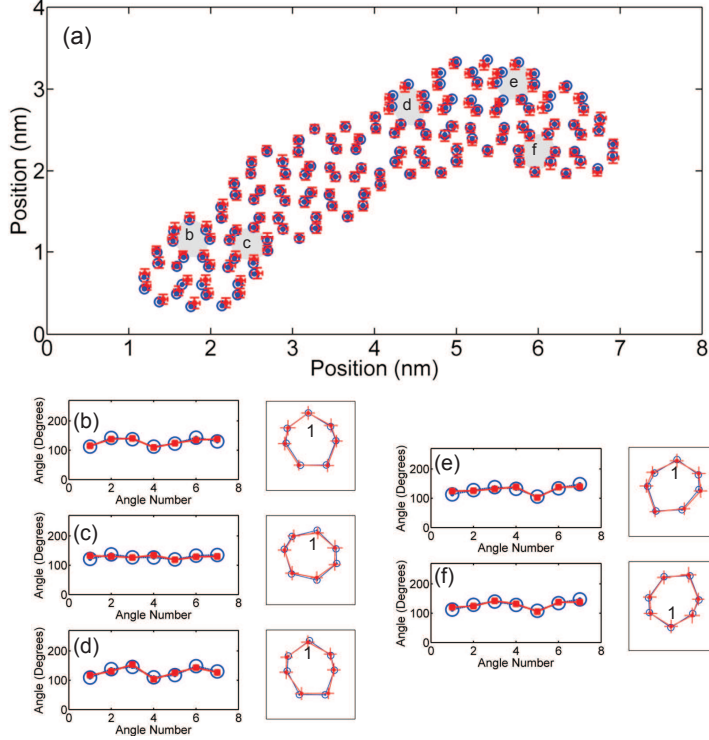


FIG. 9: (color online) (a) Structural units associated with the stepped/v-shaped defect measured from the experimental column positions and aligned to theoretical column positions. Five seven-member rings (labeled (b)–(f)) are highlighted on (a). (b)–(f) The inner angles and detailed structural comparison for the seven-member rings as labeled in (a). The boxes containing the structural comparison plots are 0.4 nm square. Plot symbols, error bars and angle number are as in Fig. 7.

V. CONCLUSIONS

We have developed an atomistic model able to describe the structural features of extended $\{311\}$ defects in silicon. The model is based on the alternate combination of interstitial and bond defect chains. Using molecular dynamics simulations, we have demonstrated that the interstitial and bond defect chains spontaneously transform into extended $\{311\}$ defects. Since the combination of these chains is an extension of the Si di-interstitial structure in $\langle 110 \rangle$ and $\langle 311 \rangle$ directions, the model presents a pathway for the formation of extended $\{311\}$ defects from simpler point defects. The model is able to reproduce both planar defects and those that show steps and bends. In fact, from the simulations we have identified a particular atomic arrangement in a $\{311\}$ defect step not previously reported.

We have been able to achieve experimental sub-ångstrom precision using unprocessed HAADF STEM images in order to compare our simulation results with experimental $\{311\}$ defect structures that show steps, bends and both. We have found very good agreement between calculated and experimental atomic positions, of the order of the average uncertainty in the experimental measurements. The model is also able to correctly predict the variation in the shape of five-, six-, seven- and eight-member rings along the $\{311\}$ defects, as well as the defect width shrinkage accounting for a more than 50% ratio between I and O units.

Acknowledgments

This work has been partially funded by the Spanish Ministerio de Ciencia e Innovación under Project No. TEC2011-27701. KJD is grateful to the Ontario Ministry of Economic Development and Innovation for partial support of a Postdoctoral Fellowship. GAB is grateful to NSERC for a Discovery Accelerator Grant partially supporting of this work. The experimental microscopy work was carried out at the Canadian Centre for Electron Microscopy, a National Facility supported by NSERC and McMaster University.

* Electronic address: lmarques@ele.uva.es

- ¹ N. E. B. Cowern, G. Mannino, P. A. Stolck, F. Roozeboom, H. G. A. Huizing, J. G. M. van Berkum, F. Cristiano, A. Claverie, and M. Jaraiz, *Phys. Rev. Lett.* **82**, 4460 (1999).
- ² S. Takeda, *Microscopy Res. Tech. B* **40**, 313 (1998).
- ³ A. Claverie, B. Colombeau, B. D. Mauduit, C. Bonafos, X. Hebras, G. B. Assayag, and F. Cristiano, *Appl. Phys. A* **76**, 1025 (2003).
- ⁴ H. Park and J. W. Wilkins, *Phys. Rev. B* **79**, 241203 (2009).
- ⁵ H. Park and J. W. Wilkins, *Appl. Phys. Lett.* **98**, 171915 (2011).
- ⁶ J. P. Goss, P. Briddon, T. A. G. Eberlein, R. Jones, N. Pinho, A. Blumenau, and S. Öberg, *Appl. Phys. Lett.* **85**, 4633 (2004).
- ⁷ W. L. Ng, M. A. Lourenco, R. M. Gwilliam, S. Ledain, G. Shao, and K. P. Homewood, *Nature* **410**, 192 (2001).
- ⁸ D. J. Eaglesham, P. A. Stolck, H.-J. Gossmann, and J. M. Poate, *Appl. Phys. Lett.* **65**, 2305

- (1994).
- ⁹ S. Takeda, Jap. J. Appl. Phys. **30**, L639 (1991).
 - ¹⁰ M. Kohyama and S. Takeda, Phys. Rev. B **46**, 12305 (1992).
 - ¹¹ S. Takeda, M. Kohyama, and K. Ibe, Philos. Mag. A **70**, 287 (1994).
 - ¹² M. Kohyama and S. Takeda, Phys. Rev. B **51**, 13111 (1995).
 - ¹³ J. Kim, J. W. Wilkins, F. S. Khan, and A. Canning, Phys. Rev. B **55**, 16186 (1997).
 - ¹⁴ P. Alippi and L. Colombo, Phys. Rev. B **62**, 1815 (2000).
 - ¹⁵ J. P. Goss, T. A. G. Eberlein, R. Jones, N. Pinho, A. Blumenau, T. Frauenheim, P. Briddon, and S. Öberg, J. Phys. Condens. Mat. **14**, 12843 (2002).
 - ¹⁶ L. A. Marqués, L. Pelaz, I. Santos, P. López, and M. Aboy, Phys. Rev. B **78**, 193201 (2008).
 - ¹⁷ K. J. Dudeck, L. A. Marqués, A. P. Knights, R. M. Gwilliam, and G. A. Botton, Phys. Rev. Lett. **110**, 166102 (2013).
 - ¹⁸ M. Tang, L. Colombo, J. Zhu, and T. D. de la Rubia, Phys. Rev. B **55**, 14279 (1997).
 - ¹⁹ F. Cargnoni, C. Gatti, and L. Colombo, Phys. Rev. B **57**, 170 (1998).
 - ²⁰ L. A. Marqués, L. Pelaz, J. Hernández, J. Barbolla, and G. H. Gilmer, Phys. Rev. B **64**, 45214 (2001).
 - ²¹ J. Tersoff, Phys. Rev. B **39**, 5566 (1989).
 - ²² F. H. Stillinger and T. A. Weber, Phys. Rev. B **31**, 5262 (1985).
 - ²³ M. Posselt, F. Gao, and D. Zwicker, Phys. Rev. B **71**, 245202 (2005).
 - ²⁴ D. A. Richie, J. Kim, S. A. Barr, K. R. A. Hazzard, R. Hennig, and J. W. Wilkins, Phys. Rev. Lett. **92**, 045501 (2004).
 - ²⁵ S. Lee and G. S. Hwang, Phys. Rev. B **78**, 045204 (2008).
 - ²⁶ S. K. Estreicher, M. Gharaibeh, P. A. Fedders, and P. Ordejón, Phys. Rev. Lett. **86**, 1247 (2001).
 - ²⁷ N. Arai, S. Takeda, and M. Kohyama, Phys. Rev. Lett. **78**, 4265 (1997).
 - ²⁸ J. W. Corbett, J. Karins, and T. Y. Tan, Nucl. Instrum. Methods **182/183**, 457 (1981).
 - ²⁹ H. G. A. Huizing, C. G. G. Viser, N. E. B. Cowern, P. A. Stolk, and R. C. M. de Kruijff, Appl. Phys. Lett. **69**, 1211 (1996).
 - ³⁰ K. J. Dudeck, E. Haunte-Ceron, A. P. Knights, R. M. Gwilliam, and G. A. Botton, Semicond. Sci. Technol. **28**, 125012 (2013).
 - ³¹ R. F. Egerton, *Electron Energy-Loss Spectroscopy in the Electron Microscopy* (Plenum, New

- York, 1996).
- ³² J. M. Haile, *Molecular Dynamics Simulations: Elementary Methods* (John Wiley & Sons, New York, 1992).
- ³³ S. Munetoh, K. Moriguchi, K. Kamei, A. Shintani, and T. Motooka, *Phys. Rev. Lett.* **86**, 4879 (2001).
- ³⁴ L. A. Marqués, L. Pelaz, M. Aboy, L. Enríquez, and J. Barbolla, *Phys. Rev. Lett.* **91**, 135504 (2003).
- ³⁵ L. A. Marqués, L. Pelaz, P. Castrillo, and J. Barbolla, *Phys. Rev. B* **71**, 085204 (2005).
- ³⁶ L. A. Marqués, L. Pelaz, P. López, I. Santos, and M. Aboy, *Phys. Rev. B* **76**, 153201 (2007).
- ³⁷ L. A. Marqués, L. Pelaz, M. Aboy, and J. Barbolla, *Nucl. Instrum. Methods Phys. Res. B* **216**, 57 (2004).
- ³⁸ C. W. Gear, *Numerical Initial Value Problems in Ordinary Differential Equations* (Prentice-Hall, Englewood Cliffs, NJ, 1971).
- ³⁹ D. Kendall, *Stat. Sci.* **4**, 87 (1989).